Understanding the Friction and Deformation Behavior of Micro/Nano-Hierarchical Textures through In-situ SEM Observation and Mechanics Modeling

Mahyar Afshar-Mohajer^{1,2}, Xingwei Yang³, Rong Long³, and Min Zou^{1,2*}

¹Department of Mechanical Engineering, University of Arkansas, Fayetteville, AR, 72701, USA

²Center for Advanced Surface Engineering, University of Arkansas, Fayetteville, AR, 72701,

USA

³Department of Mechanical Engineering, University of Colorado, Boulder, Colorado 80309,

USA

*Corresponding author, e-mail address: mzou@uark.edu

Abstract

Micro/nano-hierarchical textures play essential roles in realizing the functionalities of surfaces. Their friction and deformation behavior at the nanoscale, although important, are relatively unknown. In this study, through targeted friction tests inside a scanning electron microscope of individual micro/nano-hierarchical structures (micropillars covered with nanohairs) fabricated by two-photon lithography, we discovered the coupling between micropillar deformation and nanohair height. We also found that the bending of long nanohairs can provide assistive sliding forces, and lateral force can develop even under just normal load before sliding due to the buckling of the longer nanohairs. These findings, supported by finite element modeling of the tests, will shed light on the design of novel micro/nano-hierarchical textures to realize deformation-resistant functional surfaces with controlled friction.

Keywords: Two-Photon Lithography, In-situ SEM Tribological Testing, Micro/Nano-Hierarchical Structures, Superhydrophobic.

Introduction

Surface textures play a crucial role in imparting functionalities onto surfaces, such as superhydrophobicity [1–3], superhydrophilicity [4–6], icephobicity [7–9], low drag resistance, and high adhesion strength [10–12]. Micro/nano-hierarchical textures of surfaces in nature have been found to be indispensable for contributing to these functionalities [13].

Examples of such surfaces include superhydrophobic lotus leaves with branch-like nanostructures on top of micropapillae [14], superhydrophilic peristome of the carnivorous pitcher plant *Nepenthes alata* in the form of two-order microgrooves, enabling directional water transport [15], fish scales with low drag resistance having radially arranged micropapillae on sector-like scales of millimeter dimensions [16], and highly adhesive gecko feet with microsetae that further splits into nanoscale spatulae [17]. These hierarchical structures inspired a myriad of research activities towards studying, mimicking, and fabricating such structures to enable realization of surfaces with improved and new properties [13,18,19].

The importance of understanding the friction and deformation of micro/nano-hierarchical textures is multifold. Firstly, it can lead to the ability to tune and engineer the friction response of surfaces with the micro/nano-hierarchical textures [20–25]. Secondly, in surfaces where micro/nano-hierarchical textures are used to contribute to other functionalities such as superhydrophobicity, deformation resistance of these textures are important to determine the durability of the surfaces [26]. However, studying friction and deformation of micro/nano-hierarchical textures are challenging because of the multiscale nature and their minute size [27].

In addition to modelling and numerical simulations [20,28–32], various complementary methods have been used to overcome the inherent complexities of studying surface forces on hierarchical

structures, when tested under normal and tangential loads. A number of studies examined the deformation of hierarchical structures under external load. This has been achieved mostly via microscopy of hierarchical structures before and after testing [11,33,34]. Although some microscopy were conducted during the testing process of hierarchical textures [35–38], the smallest structures of the tested hierarchies were in a range of few microns [36,38], tens of microns [35], or hundreds of microns [37]. It should be noted that deformation of non-hierarchically patterned surfaces (e.g., fibrillar surfaces) has also been investigated through microscopy during testing [22,39–44]. These studies however, similar to the above-mentioned studies on hierarchical textures also did not include sub-micron scale structures. For example microscopy of 40 μ m × 100 μ m pillars during shear testing was done using optical microscopy with 12X magnification, [43] and in another study, even when electron microscopy was used, the tested pillars were at least 50 μ m × 10 μ m [22]. Also, a disproportionally larger number of studies are on surfaces subjected only to normal loading because friction causes more complex deformations and hence is more challenging to interpret the results [34].

In this study we performed targeted friction tests on tailor-designed individual micro/nano-hierarchical textures and gained new insights into their mechanical behavior, namely the coupling between the mechanics and deformations of different length scales as well as the frictional response of the structures, not only during the sliding of surfaces but also before sliding started. This was particularly enabled by a commercial high-resolution friction testing module placed inside a scanning electron microscope (SEM), allowing the direct observation of the interactions between the testing tip and the micro/nano-hierarchical structures. High resolution 3D printing known as two-photon lithography (TPL) [45] was used to fabricate precise micro/nano-

hierarchical textures, which enabled matching finite element modeling of the structures, leading to fundamental understanding of the mechanisms involved.

2. Experimental Methods

2.1 Fabrication of Micro/Nano-Structures Using TPL

Fig. 1 illustrates the schematics of the sample fabrication and in-situ testing and snapshots of the in-situ SEM sliding of a micro/nano-hierarchical structure under a normal load. While the fabrication section of the figure only shows a single structure as an example, the fabricated textured surfaces consisted of tens of thousands of structures.

A TPL machine (Photonic Professional GT, Nanoscribe GmbH) was used to print the micro/nano-structures. The system uses a diode-pumped, erbium-doped femtosecond fiber laser that has a 100-fs pulse width (Toptica Photonics AG). The laser has an 80 MHz repetition rate and a wavelength of 780 nm. The printing was carried out using a 63X, NA 1.4 lens, by dipping the lens inside the negative photoresist (IP-Dip, Nanoscribe GmbH), in a method known as "dip-in mode" and scanning the laser's two-photon focal point continuously along the programmed path, following the design of the micro-structure (Fig. 1(a)). The nano-pillars, referred to as nanohairs, were printed after the micro-structures were printed using the "pulsed-mode", whereby individual voxels of the two-photon laser were programmed to be placed accurately on top of the micro-pillars at different heights. This resulted in short-hair and long-hair hierarchical structures (Fig. 1(b)). The prints were then immersed in propylene glycol monomethyl ether (PGMEA) to remove the excess photoresist and were rinsed subsequently with isopropyl alcohol.

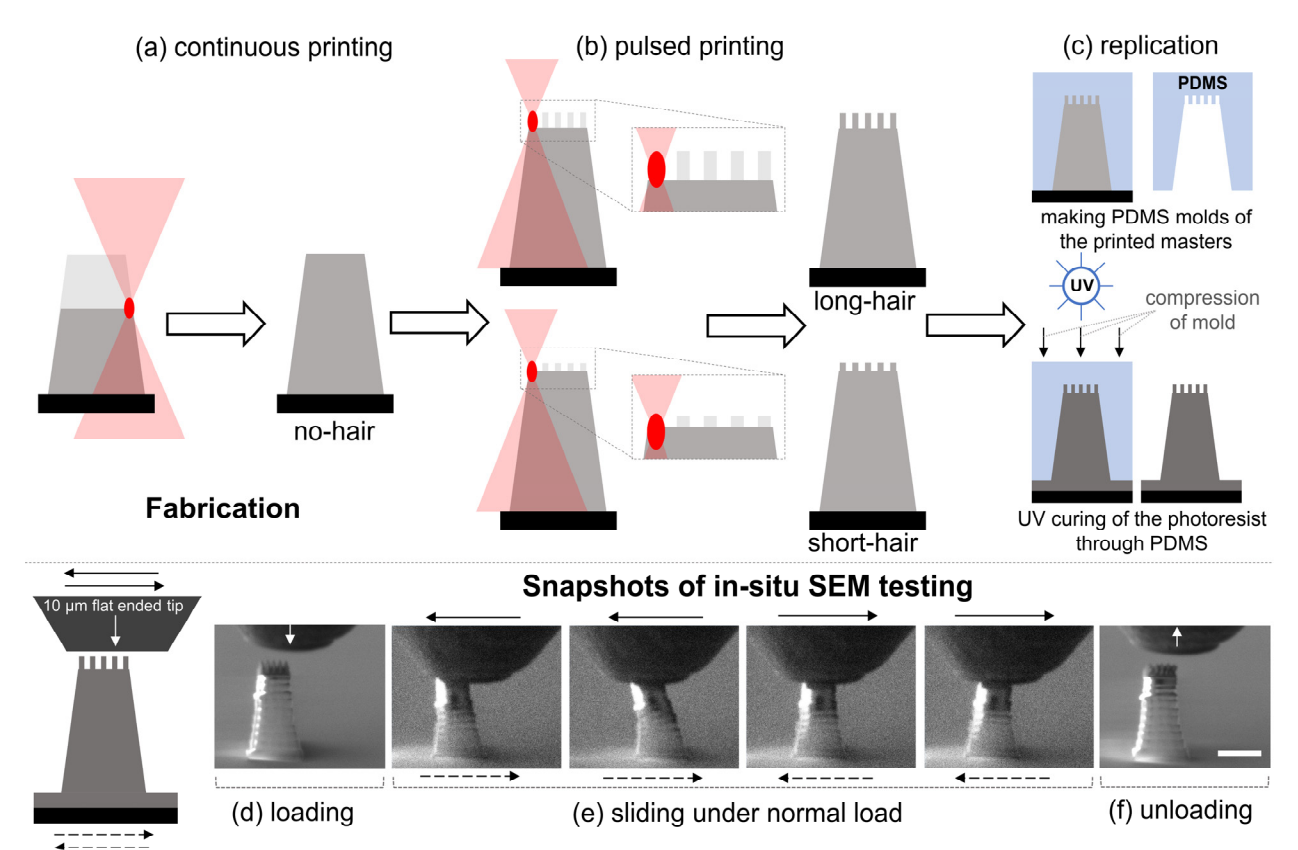


Fig. 1. Hierarchical texture fabrication and in-situ SEM testing: (a) micro-pillars were fabricated by "continuous mode" two-photon polymerization of the IP-Dip photoresist by scanning the two-photon voxel along the programmed path resulting in "no-hair" structures, (b) to form the nano-pillars on top of the printed micro-pillar, "pulsed mode" printing was carried out by individually placing the voxel at pre-determined spots (as opposed to scanning the voxel). By varying the height of the pulse placement, "long-hair" and "short-hair" structures were achieved, (c) The printed textures were replicated using soft lithography (long-hair example here). In-situ SEM testing of the structures was carried out: (d) single structures (long-hair example here) were located and loaded, (e) sliding of structures under load was enabled by lateral movement of stage in the direction of dashed arrows, resulting in the relative counterface sliding motion in the directions shown by solid arrows, and (f) load was removed (scale bar: 5 μm).

2.2 Replica Molding

Printed surfaces were used as masters to make PDMS molds. The two-part SYLGARD 184 PDMS was mixed at a 10:1 ratio utilizing a planetary centrifugal mixer (AR-100, THINKY USA Inc.). The printed masters were covered with PDMS and degassed inside a vacuum chamber to eliminate the PDMS air bubbles. The molds were then cured inside an oven overnight at 55 °C. Once fully cured, the PDMS mold was detached from the printed masters. Textured surface replication was carried out by exposing IP-Dip (Nanoscribe GmbH) photoresist to UV through the PDMS mold while layered between the PDMS mold and glass substrate under the weight of a one kilogram mass (Fig. 1(c)). The UV light (BlueWave 200, Dymax Corporation) exposure was performed at a 300 mW/cm² power density through PDMS for 600 s and then for 200 s after the mold was removed.

2.3 Silanization

Perfluorodecyltrichlorosilane (FDTS, Sigma-Aldrich Co.) vapor silanization of masters and replicated surfaces was performed to enable smooth detachment of the cured PDMS mold and make the replicated surfaces hydrophobic, respectively. Oxygen plasma treatment (PE25, Plasma Etch, Inc.) of surfaces was carried out prior to silanization for 20 s at a 150-W power and a 200-mTorr pressure.

2.4 WCA Measurement

Static and dynamic (advancing-receding) measurements of water contact angle were performed using a goniometer (OCA 15, DataPhysics Instruments USA Co.). Static WCAs were measured using 9 μ L water droplets since the deposition of smaller droplets was not possible on the long-hair textures due to the extreme hydrophobicity of the textures. Advancing-receding measurements were carried out by increasing and decreasing the volume of the droplet placed on the surface and

using the equipment's software to record the WCAs during the process. Static and advancing-receding WCA measurements were carried out on three different samples with three measurements on each sample. The measured values were averaged, and the standard error was calculated and presented as error bars.

2.5 Microscopy

Optical microscopy was used to measure the dimensions of the fabricated textures and observe the texture-water interface on water droplet-covered surfaces utilizing 3D laser scanning confocal microscopy (VK-X260K, Keyence Corp.). SEM was used to image the textured surfaces (VEGA3, TESCAN ORSAY HOLDING, a.s.).

2.6 In-situ SEM Tribology Testing

In-situ tests were performed inside an SEM (VEGA3, TESCAN ORSAY HOLDING, a.s.) using a PI-88 Picoindenter (Bruker) outfitted with a module for lateral force measurement. A conductive diamond tip with an end-diameter of 10 μm (flat-ended conical tip) was utilized as the counterface sliding against the hierarchical structures under an applied normal load of 200, 400, 600, 800, and 1000 μN, respectively. A complete sliding cycle was performed by the lateral movement of the stage 5-μm forward, followed by a 5-μm returning movement (Fig. 1(e), dashed arrows), resulting in a relative counterface sliding motion against the structures (Fig. 1(e), solid arrows). No gold sputtering was carried out on the samples used for in-situ SEM testing to avoid influencing the behavior of textures. Five in-situ SEM tribology tests were carried out on five different structures of each sample type. Since the friction tests were carried out inside the SEM in a vacuum, the humidity was negligible.

2.7 Finite Element Analysis (FEA)

FEA simulations for the deformation of micro/nano-hierarchical structures during sliding were conducted using the commercial package ABAQUS (version 2020, Simulia, Providence, RI, USA). Despite the nanoscale dimensions of the short-hair or long-hair structures, we can still apply continuum-based FEA simulations since the smallest dimensions considered here (\geq 300 nm; see Section 3.1) are still far above the atomic length scale (\sim 0.1 nm). In addition, surface effects are negligible for micro/nano-hierarchical structures, as reflected in the sub-nanometer scale elastocapillary length (i.e., the ratio between surface energy and Young's modulus; estimated with surface energy on the order of 10-100 mJ/m² and Young's modulus on the order of 1 GPa).

The FEA model consisted of two components: a rigid block to model the diamond counterface and a deformable hierarchical structure underneath the rigid block that captures the hierarchical structures used in the experiments. The structure was modeled as an elastic-plastic solid by combining a neo-Hookean hyperelastic model with a linear hardening plastic behavior. Coulomb friction model with a constant friction coefficient was used to simulate the friction of the contact interface, which is justified by three points detailed in the following. First, our tribology tests were conducted under the dry condition at a fixed loading/shear rate, and the micro/nano-pillar material was found to be elastic-plastic without significant rate-dependent behavior. Therefore, no significant rate-dependence of the friction force data was expected. Second, the tribology testing data revealed that the friction force for the no-hair structure was approximately proportional to the normal force, indicating a nearly constant friction coefficient and that the Coulomb friction model is suitable. Third, as will be discussed in Sections 3.4-3.5, the FEA simulations based on Coulomb friction were able to capture the complex behaviors of the lateral force and normal displacement

for the long-hair structure observed in the experimental data. A three-dimensional (3D) model was built for the no-hair micro-pillar and two-dimensional (2D) plane-strain models were built for the micro-pillars with nanohairs considering the dramatic increase of computational cost and difficulty in convergence of 3D simulations. Dimensions of the 3D no-hair micro-pillar were set according to experimental measurement. In the 2D models, the geometry of micro-pillar base was reduced to a trapezoid, and the nanohairs were included by adding 5 uniformly spaced rectangles on top of the micro-pillar base. A detailed description of the material parameter calibration, 3D and 2D simulations, FEA solver comparison as well as the time rescaling of FEA results is provided in the Supporting Information (Section 1 in Supplementary Material, including Figs. S1-S4).

3. Results and Discussion

3.1 Topography and Dimensions of Textured Surfaces

Fig. 2 presents SEM micrographs of the textures. In particular, Fig. 2(a-c) shows the texture arrangement of the surfaces fabricated for WCA measurements, and Fig. 2(d-f) shows the arrangement of the structures used for in-situ SEM experiments. In the samples fabricated for WCA measurements, the structures are spaced 10 μm from each other, while in the samples made for in-situ testing, the design allowed for more space between the structures (20 μm and 50 μm in the x and y direction, respectively) to enable extra freedom and avoid contact with neighboring structures, and more importantly, to provide an unobstructed view during the in-situ SEM testing of the individual structures. So, the samples fabricated for in-situ SEM testing were optimized for testing individual structures under normal and tangential loading while the samples fabricated for WCA measurements showcase the functionality of surfaces made up of such building blocks. The insets in Fig 2(d-f) show the top view of the structures. There are visible printing lines on top of

the no-hair structures (Fig 2(d)), which are formed due to the movement of the two-photon focal point along the programmed printing path.

The micro-pillars have a square cross-section, with 6 µm width at the base, 3.5 µm at the top, and 10 µm in height. In the micro/nano-hierarchical structures, A 5 by 5 array of nanohairs was fabricated on top of each micro-pillar. The nanohairs are spaced 750 nm apart and are 300 nm in diameter. Short-hair structures are 400 nm tall, and long-hair structures are 1 µm tall. These dimensions were measured by 3D laser scanning confocal microscopy.

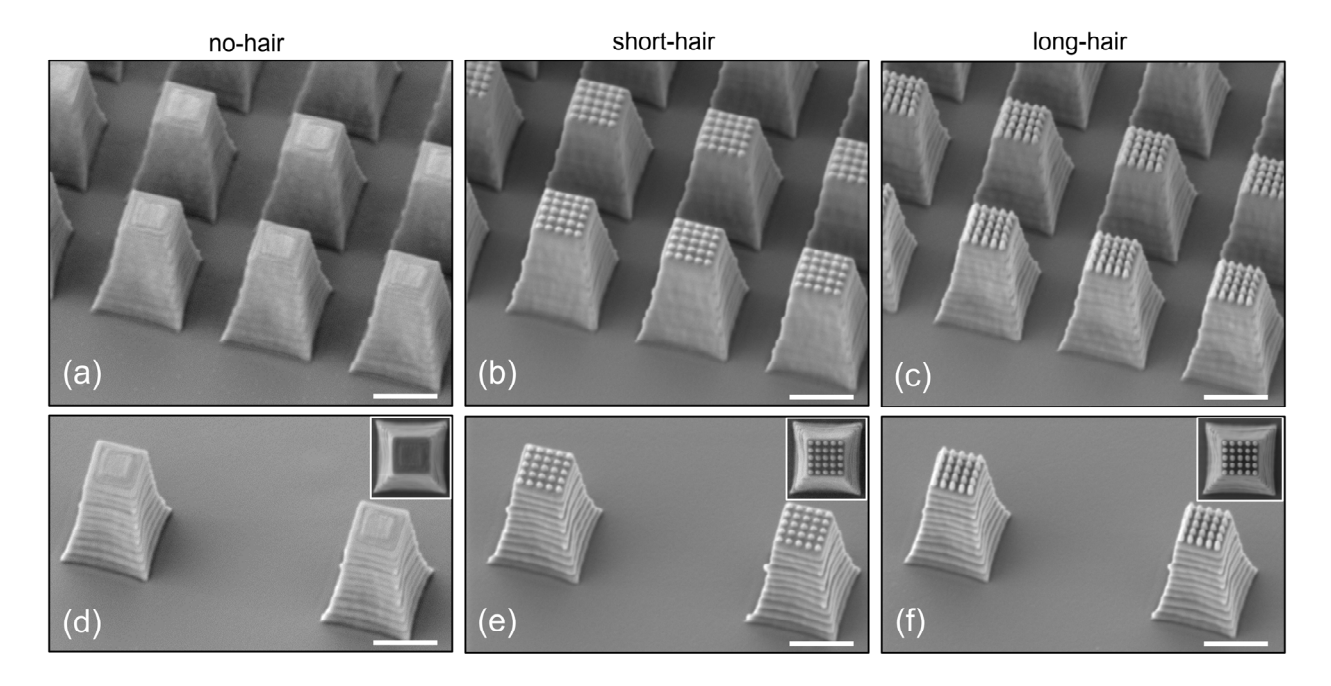


Fig. 2. SEM images of the textures: (a-c) no-hair, short-hair and long-hair structure fabricated for wettability testing, (d-f) no-hair, short-hair and long-hair structure fabricated for in-situ SEM experiments. The insets show the top view of the structures. (scale bars: 5 μm).

3.2 Hydrophobicity

Fig. 3(a) shows the static and advancing-receding WCA measurements of the textured surfaces. It should be noted that the water droplet volume had to be increased to 9 μL to obtain consistent

results since smaller droplets would not sit still on long-hair surfaces due to their superhydrophobicity. Long-hair textured surfaces had a static WCA larger than 150° ($153.5^{\circ} \pm 0.8^{\circ}$) and a very small WCA hysteresis of $3.2^{\circ} \pm 0.2^{\circ}$, demonstrating their superhydrophobicity. No-hair and short-hair surfaces, on the other hand, had static WCA values less than 150° ($144.2^{\circ} \pm 0.7^{\circ}$ and $143.9^{\circ} \pm 0.4^{\circ}$, respectively) and the WCA hysteresis values larger than 10° ($22.3^{\circ} \pm 1.0^{\circ}$ and $23.8^{\circ} \pm 1.0^{\circ}$, respectively). Therefore, they were not superhydrophobic. Surprisingly, they had very similar static and advancing-receding WCAs to each other.

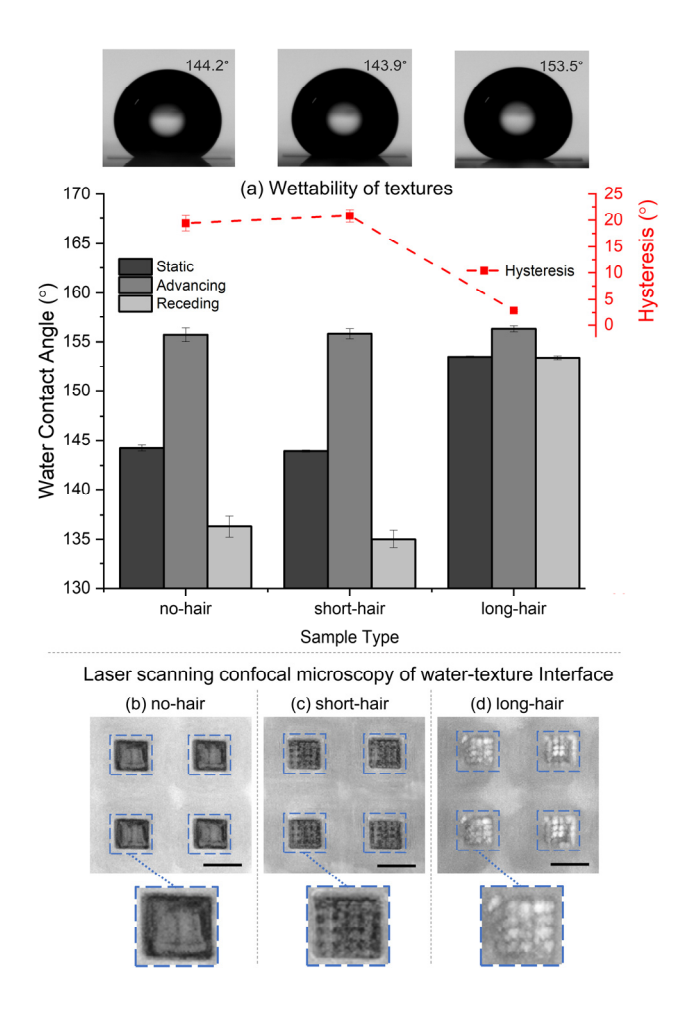


Fig. 3. Hydrophobicity of surfaces and their water-texture interfaces: (a) Water contact angle and contact angle hysteresis of the large area (3 x 3 mm) textured surfaces (error bars are standard error

of the mean). Laser scanning confocal microscopy of water-texture interface through a deposited water droplet for (b) no-hair, (c) short-hair, and (d) long-hair textures. (scale bars: 5 μm).

To obtain a better understanding of how different textures affect the wettability, laser scanning confocal microscopy was used to image the interface formed between water and the texture through a droplet deposited on the textured surfaces. Fig. 3(b-d) illustrates the Imaged interface between the top of the structures and the water droplet. The darker areas show the water-solid interface, and the whiter areas correspond to the water-air interface due to the stronger intensity of the laser light reflection [46]. For all texture types, there was a first level of air-cushion formation because of the micro-pillars (the regions outside the dashed squares), resulting in high WCAs (>140°) for all textures, despite not being superhydrophobic for the first two types. In long-hair structures, the presence of tall nanohairs on top of micro-pillars resulted in multiscale air-cushion formation, as evidenced by the significantly whiter area on the top of long-hair structures (Fig 3(d), the area inside the dashed squares). This further reduced the water-solid contact, resulting in the superhydrophobicity of the textures made up of the long-hair structures.

Laser scanning confocal microscopy of the water-texture interface also helped explain the similar range of WCAs for no-hair and short-hair textures. As observed in the surface topography section (Fig. 2(d)), the area at the top of the no-hair structures had an inherent roughness caused by the printing lines generated by the focal point movement of the two-photon laser. As shown in Fig. 3(b), this roughness affected the water-texture contact area, as is evident by the different intensities of laser reflection recorded as different gray shades. The printing lines on top of no-hair structures acted similar to the collective effect of short nano-pillars in the short-hair structures (appearing as darker dots in Fig. 3(c)). However, in both cases, the roughness/nano-pillars were

not rough/tall enough to form a second level of air-cushion as effectively as the long-hair structures.

3.3 In-Situ Lateral Force Profiles and Deformation of Structures

Fig. 4 shows the representative lateral force profiles of the structures plotted against lateral displacement when tested in-situ under the smallest and the largest applied normal loads, namely 400 μ N and 1000 μ N, respectively, during one complete forward and backward sliding cycle. The SEM images are snapshots of the structures at the end of the forward stroke of the tests, as marked on the friction profile plots as i and ii, corresponding to the 400 μ N and 1000 μ N test, respectively.

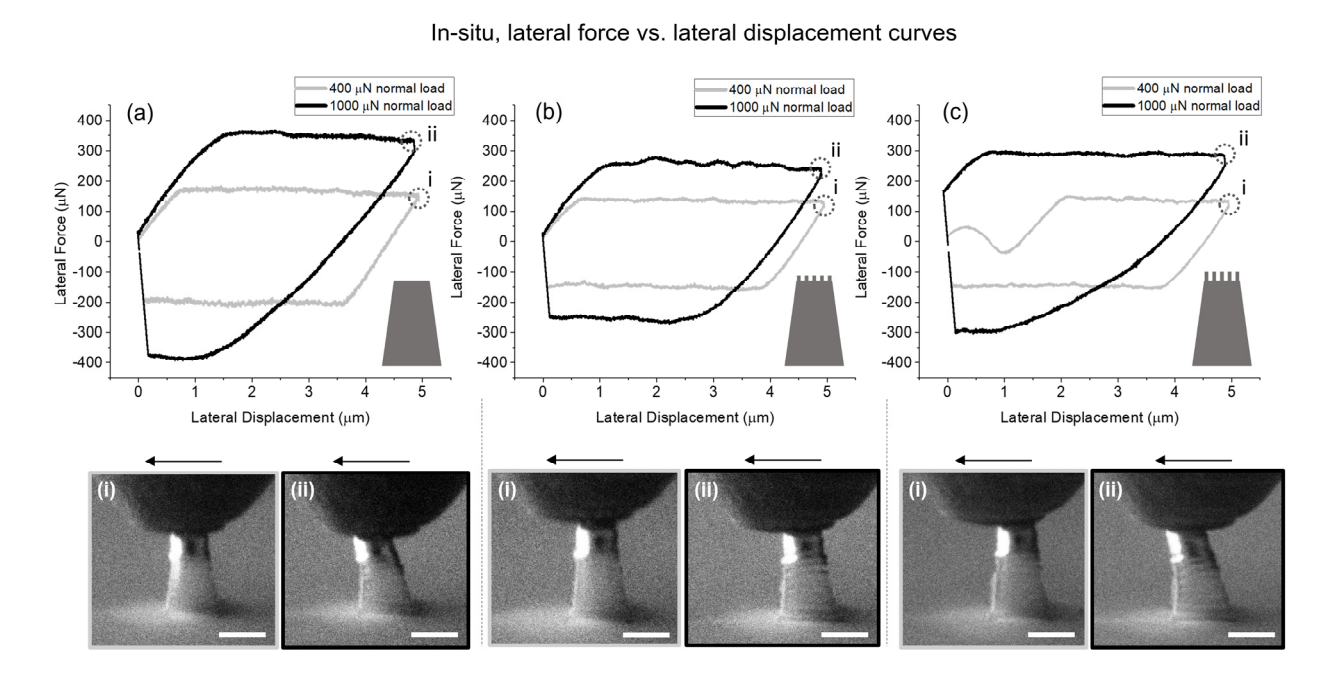


Fig. 4. Lateral force profile and the maximum bending of the structures at 400 μ N and 1000 μ N applied normal loads for (a) no-hair, (b) short-hair, and (c) long-hair structures. (arrows represent the sliding direction of the counterface against the structures during the forward stroke, scale bars: 5 μ m).

At 400 μN normal load, no significant bending of the micro-pillars was observed (Fig. 4(a.i), 4(b.i), and 4(c.i)), while as the normal load was increased to 1000 μN, bending became observable. The bending was obvious for the no-hair (Fig. 4(a.ii)) and long-hair (Fig. 4(c.ii)) structures, while the short-hair (Fig 4(b.ii)) structure only showed minor bending. This indicates the first-level structure (nanohairs) with different heights affected the deformation of the second-level structure (micro-pillars). The more severe bending observed for the no-hair and long-hair structures is consistent with the higher lateral force during sliding measured for these two structures than the short-hair structure. In other words, higher lateral force leads to larger bending of micro-pillar base. To understand the difference in lateral force, we note that the actual area of contact at the interface depends on the nanohair structure. The short-hair structure should have a smaller area of contact compared to that of the no-hair structure due to the spacing between the short hairs. The long hairs can undergo buckling, resulting in increased area of contact between the buckled hairs and the counterface compared to that of the short-hair structure, and this will be discussed and illustrated later.

The lateral force profile of long-hair structures showed unique patterns such as the dipping signature seen in the lateral force when tested under the 400 μ N normal load (grey curve, Fig. 4(c)). Similar behavior were also present when testing under 1000 μ N normal load. However, they are not observable in Fig. 4(c) (black curve) because this signature occurred before the sliding started. A detailed analysis of these signatures and their origins is provided in the following sections for the two different loading conditions namely the small normal load (400 μ N) and the large normal load (1000 μ N).

3.4 Bending of Long Hairs During Sliding Under Small Normal Load

To understand the unique dipping signatures observed in the lateral force profile of the long-hair structures in the forward stroke of the tests (Fig. 4(c)), an in-depth analysis of the experimental data was carried out, accompanied by FEA modeling of the tests. Fig. 5(a) and 5(e) show experimental and modeling lateral force profiles of the forward stroke under 400 μN normal load, plotted against time to reveal more information. In these figures, negative lateral forces imply assistance to sliding, while positive lateral forces are due to the resistance to the motion [47]. Fig. 5(b) and 5(f) show the normal displacement of the counterface corresponding to the lateral force profiles in Fig. 5(a) and 5(e), respectively. Fig. 5(c) shows the inputs of the in-situ test, namely the applied normal load (blue) and the lateral displacement (red). Fig. 5(d) shows the in-situ SEM snapshots of the deformation of the long-hair structure (top of structure magnified) corresponding to specific events 2, 3, 4, 5 marked in Fig. 5(a) and 5(b), and Fig. 5(g) illustrates the modeled long-hair structure and its deformations, corresponding to specific events 2, 3, 4, 5, marked in Fig. 5(e) and 5(f). The unique dipping signatures of lateral force seen in Fig. 5(a) and 5(e) were also observed in our previous study when testing textures with a high aspect ratio [48].

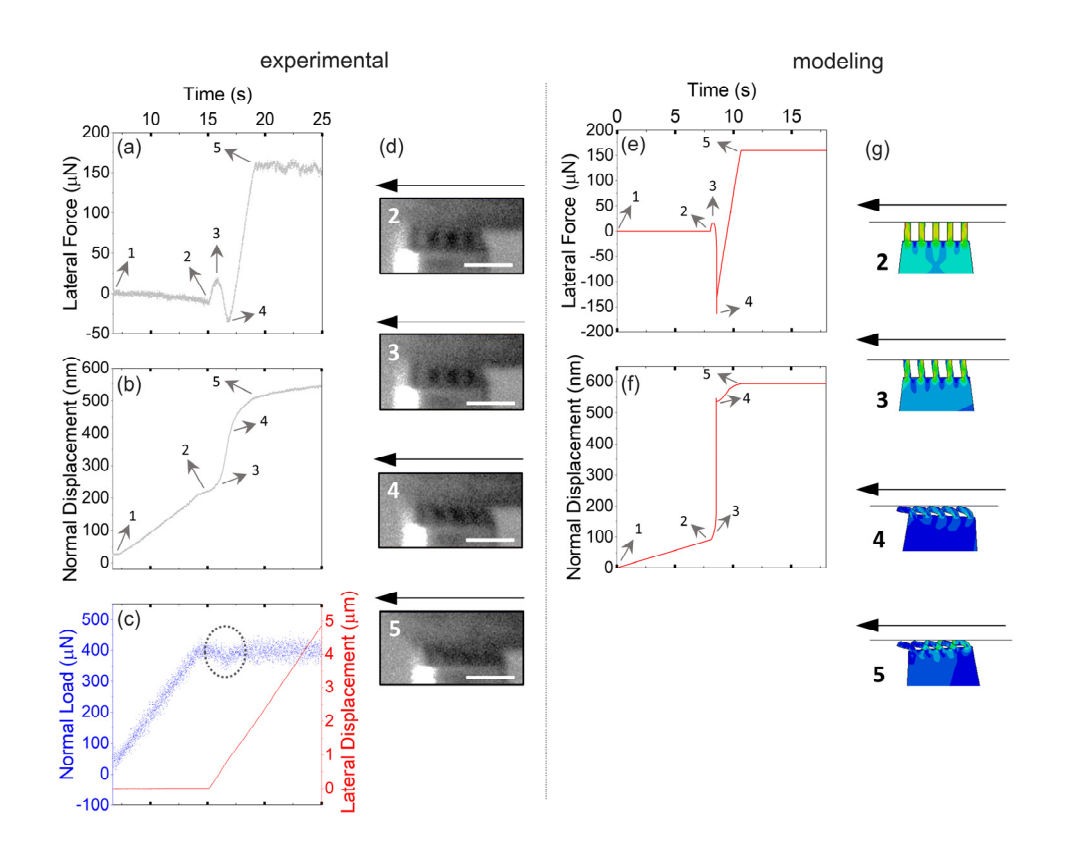


Fig. 5. Bending of long hairs after sliding and its effect on the lateral force and normal displacement obtained from experiments and modeling: (a,e) lateral forces, (b,f) normal displacements of counterface, (c) applied normal load and lateral displacement during the test, and (d,g) in-situ snapshot and modeling of long-hair structure corresponding to the marked events in the plots (leftward arrows show the sliding direction of counterface. Scale bars: $2 \mu m$).

Initial normal displacement of the structures is observed in Fig. 5(b) and 5(f) as the application of normal load started at point 1 and before the sliding started. As the targeted normal load was reached at point 2, the lateral movement began. As shown in Fig. 5(a) and Fig. 5(e), the initial resistance of the long hairs to sliding resulted in a positive lateral force (resistive force) between points 2 and 3, reaching its maximum value at point 3. Further sliding beyond point 3 caused collapse of the long hairs as they bent in the sliding direction as can be directly observed with the help of in-situ SEM snapshot (Fig. 5(d), point 4). This is also evidenced by the sudden normal

displacement increase between points 3 and 4 (Fig. 5(b) and 5(f)), the modeled deformation depicted in Fig. 5(g) (point 4), and also the transitory dip in the normal load shown in Fig. 5(c) inside the dotted circle. Bending of the long hairs in the same direction as sliding resulted in assistive forces and hence a negative lateral force between points 3 and 4. As the assistive sliding ended, the contact area between the tip and structure increased due to the bent hairs (point 4), and the lateral force became resistive (positive) and stabilized (point 5) until the end of the forward stroke. Video S1, provided in the Supplementary Material, contains the recorded video of the insitu SEM testing from which the data and snapshots in Fig. 5(a-d) are taken.

3.5 Pre-Sliding Buckling of Long Hairs Under Large Normal Load

At high normal loads, the long hairs underwent buckling before the start of sliding. Different scenarios of such buckling (based on the buckling direction), which occurred under 1000 µN normal load, are presented here. Fig. 6 illustrates the buckling of long hairs in the sliding direction and opposite to the sliding direction of counterface and how it affected the lateral force and normal displacement, as captured both experimentally and via modeling. Plotting the forces and displacements against time was especially crucial in this case to unravel the pre-sliding events that were obscured when plotted against lateral displacement.

Fig. 6. Buckling of long hairs under normal load in different directions and its effect on the lateral force and normal displacement obtained experimentally and via modeling: (a-h) experimental and modeling results of buckling in the counterface sliding direction, and (i-p) experimental and modeling results of buckling in the opposite direction to counterface sliding. (scale bars: 2 μm).

In both cases, an initial normal displacement was seen due to the application of normal load (starting at point 1), as shown in Fig. 6(b), 6(f), 6(j), and 6(n). Between the onset of buckling (point 2) and its completion (point 3), an increase in the normal displacement occurred, caused by the collapse of the long hairs. Interestingly, the lateral force changed even before sliding started (points

2 to 3 in Fig. 6(a), 6(e), 6(i), and 6(m)). This was caused by either assistive or resistive forces that the buckled hairs exerted. From Fig. 6(g), it can be seen that buckling in the sliding direction of counterface resulted in negative lateral force between points 2 and 3 (Fig. 6(a) and 6(e)) due to exertion of assistive lateral force, similar to the post-sliding bending of the hairs observed in Fig. 5. However, as shown in Fig. 6(o) (point 3), when buckling direction is opposite to the sliding direction, the lateral force curve showed the development of positive force (Fig. 6(i) and 6(m)) due to the resistive lateral force that the hairs exerted. Once sliding started, there was only resistance to the sliding, as the deformation of long hairs had already occurred. Hence, the potential assistive force was exhausted, resulting in positive lateral forces until the end of the forward motion at point 4.

Another phenomenon that accompanied the pre-sliding nanohair buckling was the bending of the micro-pillar, showing that the first-level structure deformation (nanohair buckling) under normal load only can induce the bending of the second-level structure (micro-pillar) in the long-hair hierarchical structures, as shown in Fig. 6(g.3) and 6(o.3). The magnified view of the pre-sliding region of lateral displacement in Fig. 6(d) and 6(l) shows that the nanohair-buckling-induced deformation of micro-pillar base resulted in small pre-sliding lateral displacements in two opposite directions.

Fig. 6(h) and 6(p) show the SEM images of the structures after the experimental tests, corresponding to the two cases with opposing buckling directions that resulted in the deformation of the long hairs in opposite directions.

It is also possible for the nanohairs to buckle in a direction in between the two directions discussed, e.g. closer to perpendicular to the sliding direction, which results in pre-sliding lateral forces very close to zero since the collapse of hairs is neither in the sliding direction (assistive) nor

opposite to it (resistive). This kind of buckling was also observed in the experiments and its effect on lateral force is shown in Fig. S8 in the Supplementary Material.

3.6 Friction of the Structures

Friction is proportional to the real area of contact, and a larger contact area between two interacting surfaces results in higher friction [49]. Fig. 7 summarizes friction values of the different types of structures under the normal load from 400 μ N to 1000 μ N during the forward and backward strokes of the one-cycle test (Fig. 4). The friction values were the average of 5 measurements extracted from the plateaued part of the lateral force profile during the forward and backward stroke, respectively. The error bars show the standard error.

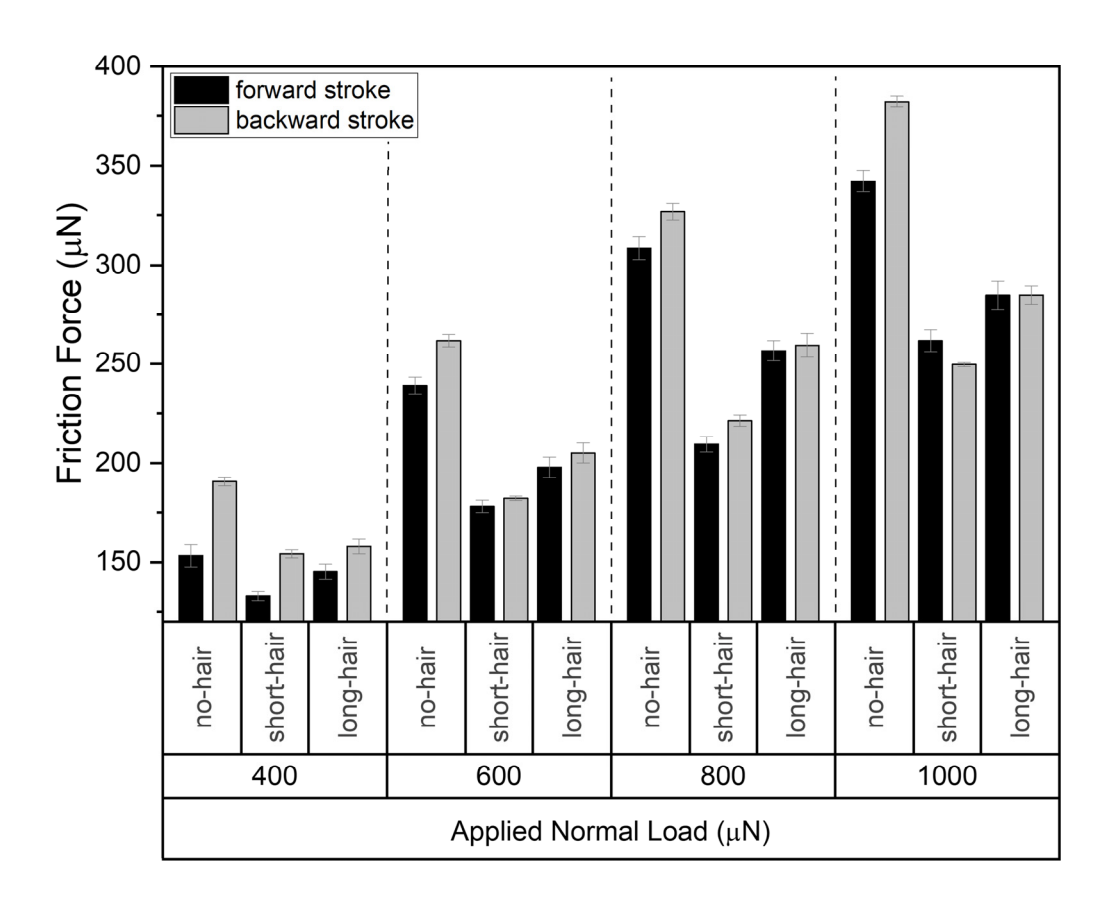


Fig. 7. Average values of friction force of structures as a function of applied normal load during both the forward and backward strokes of the one-cycle test. (error bars are standard error of the mean).

Looking at the friction force during the forward stroke in Fig. 7, it can be seen that the no-hair structures had the highest friction, which became more pronounced as the normal load increased. The short-hair structures showed the lowest friction, and the long-hair structures had friction values in between. This was expected since no-hair structures had the highest area of contact with the counterface, while the nanohairs reduced the contact area especially in the case of short-hair structures. The friction value of the no-hair structure was closest to the other structures under the smallest normal load (400 µN) due to the printing lines on the top of no-hair structures (Fig. 2d) acting as roughness, which reduced the contact area. However, as the normal load increased, the difference between the friction of no-hair structures and the other structures increased due to flattening of the surface under normal load and the resulting increase in the contact area. Taller hairs of the long-hair structures were prone to deformation due to bending (Fig. 5) or buckling (Fig. 6), which resulted in an increased contact area relative to short-hair structures. The friction of hierarchical structures was hence a function of the evolution of their contact area as a result of the susceptibility of their components to deformation. It should be noted that while here no-hair structures showed higher friction than long-hair structures, both increased and reduced friction have been reported on fibrillar patterns comparing to flat controls [50]. This has been attributed to the bending and buckling of fibrillar structures which reduced the contact area in the studies where they showed reduced friction [34,43,51].

Fig. 7 shows that there are differences in the friction values between the forward and backward strokes, with the friction during the backward stroke being higher for most of them. This is due to the deformation of the top surface of the structures (the printing lines of the no-hair structures and the nanohairs of the short- and long-hair structures) during the forward stroke, resulting in an increased true contact area during the backward stroke. At higher normal loads, for the structures with nanohairs, severe deformation of the short hairs and buckling of long hairs occurred during the forward stroke, which led to less change in the true contact area during the backward stroke and thus reduced friction anisotropy. For the no-hair structures, however, the anisotropy remained at higher normal loads because the printing lines on top of the no-hair structures continued to deform after the forward stroke. It should be noted that observation of different forward and backward friction values is common at the microscale [52].

4. Conclusions

Enabled by the resolution and accuracy of TPL, hierarchical structures were fabricated. The effect of increasing the height of the first-level structure of the hierarchy (nanohairs) in achieving superhydrophobicity was directly observed through laser scanning confocal microscopy of the interface. This is facilitated by forming a multiscale air cushion at the interface between the surface and the droplet.

The fabrication accuracy was matched with the accuracy of the small-scale tribological testing of the textures inside an SEM, which not only enabled precise targeting of individual hierarchical structures but also provided direct observation of their deformation. This resulted in the observation of unique phenomena due to the hierarchy, such as the coupling effect of the first-level structure (nanohair) deformation to the bending of the second-level structure (micro-pillar

base) before or after sliding was initiated. Specifically, different nanohair heights affected the contact area, and hence the lateral force and the degree of micro-pillar bending (Section 3.3). Moreover, the buckling of the long hairs caused a lateral force to bend the micro-pillar (Section 3.5). Another interesting phenomenon observed is that the bending and buckling of the long-hair structures resulted in assistive forces for sliding and hence negative lateral force. This could happen, even before the start of programmed sliding in the case of buckling of long-hair structures.

This level of control and accuracy over fabrication and testing offers a great path for studying hierarchical textures, which cannot be accomplished by bulk testing methods. This approach enables a fundamental understanding of the surfaces at their individual building blocks level, which when paired with computational models, will lead to better engineering of textured functional surfaces.

Acknowledgements

The research was supported by the U.S. National Science Foundation (NSF) under Grant No. CMS-1463306 and the Center for Advanced Surface Engineering under Grant No. OIA-1457888 and the Arkansas EPSCoR Program, ASSET III. The authors thank the Arkansas Biosciences Institute and the University of Arkansas for major equipment funding support. X.Y. and R.L. are supported by a CAREER award from the National Science Foundation (NSF CMMI-1752449).

References

- [1] Gogte S, Vorobieff P, Truesdell R, Mammoli A, van Swol F, Shah P, et al. Effective slip on textured superhydrophobic surfaces. Phys Fluids 2005;17:51701. https://doi.org/10.1063/1.1896405.
- [2] McHale G, Shirtcliffe NJ, Newton MI. Contact-Angle Hysteresis on Super-Hydrophobic Surfaces. Langmuir 2004;20:10146–9. https://doi.org/10.1021/la0486584.
- [3] Maitra T, Tiwari MK, Antonini C, Schoch P, Jung S, Eberle P, et al. On the Nanoengineering of Superhydrophobic and Impalement Resistant Surface Textures below the Freezing Temperature. Nano Lett 2014;14:172–82. https://doi.org/10.1021/nl4037092.
- [4] Li B, Li H, Huang L, Ren N, Kong X. Femtosecond pulsed laser textured titanium surfaces with stable superhydrophilicity and superhydrophobicity. Appl Surf Sci 2016;389:585–93. https://doi.org/https://doi.org/10.1016/j.apsusc.2016.07.137.
- [5] Palumbo F, Di Mundo R, Cappelluti D, d'Agostino R. SuperHydrophobic and SuperHydrophilic Polycarbonate by Tailoring Chemistry and Nano-texture with Plasma Processing. Plasma Process Polym 2011;8:118–26. https://doi.org/10.1002/ppap.201000098.
- [6] Drelich J, Chibowski E. Superhydrophilic and Superwetting Surfaces: Definition and Mechanisms of Control. Langmuir 2010;26:18621–3. https://doi.org/10.1021/la1039893.
- [7] Lv J, Song Y, Jiang L, Wang J. Bio-Inspired Strategies for Anti-Icing. ACS Nano 2014;8:3152–69. https://doi.org/10.1021/nn406522n.
- [8] Shen Y, Wang G, Tao J, Zhu C, Liu S, Jin M, et al. Anti-Icing Performance of

- Superhydrophobic Texture Surfaces Depending on Reference Environments. Adv Mater Interfaces 2017;4:1700836. https://doi.org/10.1002/admi.201700836.
- [9] Meuler AJ, McKinley GH, Cohen RE. Exploiting Topographical Texture To Impart Icephobicity. ACS Nano 2010;4:7048–52. https://doi.org/10.1021/nn103214q.
- [10] Fleming RA, Zou M. Nanostructure-Textured Surfaces with Low Friction and High Deformation Resistance. Tribol Trans 2018;61:80–7. https://doi.org/10.1080/10402004.2016.1274066.
- [11] Rong Z, Zhou Y, Chen B, Robertson J, Federle W, Hofmann S, et al. Bio-Inspired Hierarchical Polymer Fiber–Carbon Nanotube Adhesives. Adv Mater 2014;26:1456–61. https://doi.org/10.1002/adma.201304601.
- [12] Iturri J, Xue L, Kappl M, García-Fernández L, Barnes WJP, Butt H-J, et al. Torrent Frog-Inspired Adhesives: Attachment to Flooded Surfaces. Adv Funct Mater 2015;25:1499–505. https://doi.org/10.1002/adfm.201403751.
- [13] Bae W-G, Kim HN, Kim D, Park S-H, Jeong HE, Suh K-Y. 25th Anniversary Article: Scalable Multiscale Patterned Structures Inspired by Nature: the Role of Hierarchy. Adv Mater 2014;26:675–700. https://doi.org/10.1002/adma.201303412.
- [14] Feng L, Li S, Li Y, Li H, Zhang L, Zhai J, et al. Super-Hydrophobic Surfaces: From Natural to Artificial. Adv Mater 2002;14:1857–60. https://doi.org/10.1002/adma.200290020.
- [15] Chen H, Zhang P, Zhang L, Liu H, Jiang Y, Zhang D, et al. Continuous directional water transport on the peristome surface of Nepenthes alata. Nature 2016;532:85–9. https://doi.org/10.1038/nature17189.

- [16] Liu M, Wang S, Wei Z, Song Y, Jiang L. Bioinspired Design of a Superoleophobic and Low Adhesive Water/Solid Interface. Adv Mater 2009;21:665–9. https://doi.org/https://doi.org/10.1002/adma.200801782.
- [17] Liu K, Du J, Wu J, Jiang L. Superhydrophobic gecko feet with high adhesive forces towards water and their bio-inspired materials. Nanoscale 2012;4:768–72. https://doi.org/10.1039/C1NR11369K.
- [18] Brodoceanu D, Bauer CT, Kroner E, Arzt E, Kraus T. Hierarchical bioinspired adhesive surfaces—a review. Bioinspir Biomim 2016;11:51001. https://doi.org/10.1088/1748-3190/11/5/051001.
- [19] Gogolides E, Ellinas K, Tserepi A. Hierarchical micro and nano structured, hydrophilic, superhydrophobic and superoleophobic surfaces incorporated in microfluidics, microarrays and lab on chip microsystems. Microelectron Eng 2015;132:135–55. https://doi.org/https://doi.org/10.1016/j.mee.2014.10.002.
- [20] Costagliola G, Bosia F, Pugno NM. Tuning friction with composite hierarchical surfaces.

 Tribol Int 2017;115:261–7. https://doi.org/https://doi.org/10.1016/j.triboint.2017.05.012.
- [21] Gachot C, Rosenkranz A, Hsu SM, Costa HL. A critical assessment of surface texturing for friction and wear improvement. Wear 2017;372–373:21–41. https://doi.org/https://doi.org/10.1016/j.wear.2016.11.020.
- [22] Murarash B, Itovich Y, Varenberg M. Tuning elastomer friction by hexagonal surface patterning. Soft Matter 2011;7:5553. https://doi.org/10.1039/c1sm00015b.
- [23] Li N, Xu E, Liu Z, Wang X, Liu L. Tuning apparent friction coefficient by controlled

- patterning bulk metallic glasses surfaces. Sci Rep 2016;6:39388. https://doi.org/10.1038/srep39388.
- [24] Dickrell PL, Sinnott SB, Hahn DW, Raravikar NR, Schadler LS, Ajayan PM, et al. Frictional anisotropy of oriented carbon nanotube surfaces. Tribol Lett 2005;18:59–62. https://doi.org/10.1007/s11249-004-1752-0.
- [25] Grützmacher PG, Profito FJ, Rosenkranz A. Multi-Scale Surface Texturing in Tribology—
 Current Knowledge and Future Perspectives. Lubr 2019;7.
 https://doi.org/10.3390/lubricants7110095.
- [26] Nosonovsky M, Bhushan B. Multiscale friction mechanisms and hierarchical surfaces in nano- and bio-tribology. Mater Sci Eng R Reports 2007;58:162–93. https://doi.org/http://dx.doi.org/10.1016/j.mser.2007.09.001.
- [27] Genin GM. Integrated Multiscale Biomaterials Experiment and Modeling. ACS Biomater Sci Eng 2017;3:2628–32. https://doi.org/10.1021/acsbiomaterials.7b00821.
- [28] Signetti S, Bosia F, Pugno NM. Computational modeling of the mechanics of hierarchical materials. MRS Bull 2016;41:694–9. https://doi.org/10.1557/mrs.2016.185.
- [29] Kim TW, Bhushan B. Effect of stiffness of multi-level hierarchical attachment system on adhesion enhancement. Ultramicroscopy 2007;107:902–12. https://doi.org/https://doi.org/10.1016/j.ultramic.2006.11.008.
- [30] Costagliola G, Bosia F, Pugno NM. Hierarchical Spring-Block Model for Multiscale Friction Problems. ACS Biomater Sci Eng 2017;3:2845–52. https://doi.org/10.1021/acsbiomaterials.6b00709.

- [31] Costagliola G, Bosia F, Pugno NM. Static and dynamic friction of hierarchical surfaces. Phys Rev E 2016;94:63003. https://doi.org/10.1103/PhysRevE.94.063003.
- [32] Berardo A, Pugno NM. A model for hierarchical anisotropic friction, adhesion and wear. Tribol Int 2020;152:106549. https://doi.org/https://doi.org/10.1016/j.triboint.2020.106549.
- [33] Asbeck A, Dastoor S, Parness A, Fullerton L, Esparza N, Soto D, et al. Climbing rough vertical surfaces with hierarchical directional adhesion. 2009 IEEE Int. Conf. Robot. Autom., 2009, p. 2675–80. https://doi.org/10.1109/ROBOT.2009.5152864.
- [34] Cho Y, Minsky HK, Jiang Y, Yin K, Turner KT, Yang S. Shear Adhesion of Tapered Nanopillar Arrays. ACS Appl Mater Interfaces 2018;10:11391–7. https://doi.org/10.1021/acsami.8b02303.
- [35] Kasem H, Tsipenyuk A, Varenberg M. Biomimetic wall-shaped hierarchical microstructure for gecko-like attachment. Soft Matter 2015;11:2909–15. https://doi.org/10.1039/C4SM01916D.
- [36] Murphy MP, Kim S, Sitti M. Enhanced Adhesion by Gecko-Inspired Hierarchical Fibrillar Adhesives. ACS Appl Mater Interfaces 2009;1:849–55. https://doi.org/10.1021/am8002439.
- [37] Bauer CT, Kroner E, Fleck NA, Arzt E. Hierarchical macroscopic fibrillar adhesives: in situ study of buckling and adhesion mechanisms on wavy substrates. Bioinspir Biomim 2015;10:66002. https://doi.org/10.1088/1748-3190/10/6/066002.
- [38] Zimmer K, Zajadacz J, Lorenz P, Mayer A, Papenheim M, Scheer H-C. Shear force measurement of actuated, gecko-inspired adhesion elements with hierarchical

- polydimethylsiloxane pattern. J Micromechanics Microengineering 2020;30:25008. https://doi.org/10.1088/1361-6439/ab60bd.
- [39] Murarash B, Varenberg M. Tribometer for In Situ Scanning Electron Microscopy of Microstructured Contacts. Tribol Lett 2011;41:319–23. https://doi.org/10.1007/s11249-010-9717-y.
- [40] Liu J, Hui C-Y, Shen L, Jagota A. Compliance of a microfibril subjected to shear and normal loads. J R Soc Interface 2008;5:1087–97. https://doi.org/10.1098/rsif.2007.1336.
- [41] Kim J-K, Varenberg M. Biomimetic wall-shaped adhesive microstructure for shear-induced attachment: the effects of pulling angle and preliminary displacement. J R Soc Interface 2017;14:20170832. https://doi.org/10.1098/rsif.2017.0832.
- [42] Shen L, Jagota A, Hui C-Y. Mechanism of Sliding Friction on a Film-Terminated Fibrillar Interface. Langmuir 2009;25:2772–80. https://doi.org/10.1021/la803390x.
- [43] Varenberg M, Gorb S. Shearing of fibrillar adhesive microstructure: friction and shear-related changes in pull-off force. J R Soc Interface 2007;4:721–5. https://doi.org/10.1098/rsif.2007.0222.
- [44] Varenberg M, Gorb S. Close-up of mushroom-shaped fibrillar adhesive microstructure: contact element behaviour. J R Soc Interface 2008;5:785–9. https://doi.org/10.1098/rsif.2007.1201.
- [45] Bückmann T, Stenger N, Kadic M, Kaschke J, Frölich A, Kennerknecht T, et al. Tailored 3D Mechanical Metamaterials Made by Dip-in Direct-Laser-Writing Optical Lithography. Adv Mater 2012;24:2710–4. https://doi.org/10.1002/adma.201200584.

- [46] Luo C, Zheng H, Wang L, Fang H, Hu J, Fan C, et al. Direct Three-Dimensional Imaging of the Buried Interfaces between Water and Superhydrophobic Surfaces. Angew Chemie Int Ed 2010;49:9145–8. https://doi.org/10.1002/anie.201002470.
- [47] Chen Z, Khajeh A, Martini A, Kim SH. Identifying Physical and Chemical Contributions to Friction: A Comparative Study of Chemically Inert and Active Graphene Step Edges.

 ACS Appl Mater Interfaces 2020;12:30007–15. https://doi.org/10.1021/acsami.0c08121.
- [48] Afshar-Mohajer M, Zou M. Multi-Scale In Situ Tribological Studies of Surfaces with 3D Textures Fabricated via Two-Photon Lithography and Replica Molding. Adv Mater Interfaces 2020;7:2000299. https://doi.org/10.1002/admi.202000299.
- [49] Burton Z, Bhushan B. Hydrophobicity, adhesion, and friction properties of nanopatterned polymers and scale dependence for micro- and nanoelectromechanical systems. Nano Lett 2005;5:1607–13. https://doi.org/10.1021/nl050861b.
- [50] Xue L, Iturri J, Kappl M, Butt H-J, del Campo A. Bioinspired Orientation-Dependent Friction. Langmuir 2014;30:11175–82. https://doi.org/10.1021/la502695d.
- [51] Hui C-Y, Glassmaker NJ, Tang T, Jagota A. Design of biomimetic fibrillar interfaces: 2.

 Mechanics of enhanced adhesion. J R Soc Interface 2004;1:35–48.

 https://doi.org/10.1098/rsif.2004.0005.
- [52] Bhushan B. Nanotribology and nanomechanics. Wear 2005;259:1507–31. https://doi.org/https://doi.org/10.1016/j.wear.2005.01.010.

Supplementary Material

Understanding the Friction and Deformation Behavior of Micro/Nano-Hierarchical Textures through In-situ SEM Observation and Mechanics Modeling

Mahyar Afshar-Mohajer^{1,2}, Xingwei Yang³, Rong Long³, and Min Zou^{1,2*}

¹Department of Mechanical Engineering, University of Arkansas, Fayetteville, AR, 72701, USA

²Center for Advanced Surface Engineering, University of Arkansas, Fayetteville, AR, 72701,

USA

³Department of Mechanical Engineering, University of Colorado, Boulder, Colorado 80309, USA

^{*}Corresponding author, e-mail address: mzou@uark.edu

S1. Finite Element Analysis (FEA)

FEA simulations for the deformation of hierarchical micro-/nano-structures during sliding were conducted using the commercial package ABAQUS (version 2020, Simulia, Providence, RI, USA). The FEA model consisted of two components: a rigid block to model the diamond indenter and a deformable hierarchical structure underneath the rigid block that captures the structures used in the experiments (i.e., no-hair, short-hair, or long-hair).

Material parameters

We modelled the hierarchical micro-/nano-structures (the IP-Dip photoresist polymer that was used to fabricate the structures) as an elastic-plastic solid. The elastic component was modelled as a neo-Hookean solid with a Young's modulus of 2.6 GPa [1], and a Poisson's ratio of 0.49 [1]. The plastic component was modelled using a linear isotropic hardening behavior, and the parameters were extracted from micro tensile data available in Rohbeck et al. [1]. Fig. S1(a) shows the true stress-strain response (i.e., the Cauchy stress and logarithmic strain) of a micro tensile test extracted from Rohbeck[1]. We used the initial part of the curve to fit for a plasticity model (tensile strain $<\sim15\%$), thus approximated the elastic component using a linear relation and calculate the plastic strain $\epsilon_{\rm pl}$ using the following equation:

$$\varepsilon_{pl} = \varepsilon_{tr} - \frac{\sigma_{tr}}{E} \tag{S1}$$

where E is the Young's modulus. The data of true stress σ_{tr} versus plastic strain ϵ_{pl} is plotted in Fig. S1(b). By fitting the data with a linear hardening relation, we find that true yield stress is 80 MPa and the slope of the linear fit is 300 MPa, which were used the FEA model. The ultimate strength of the material was set to be 600 MPa.

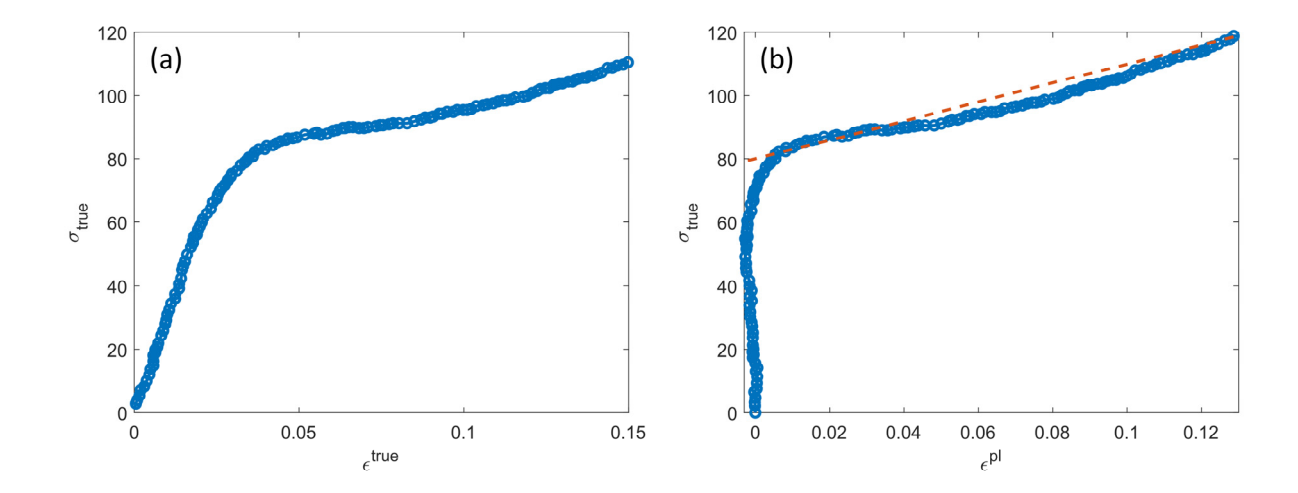


Fig. S1. (a) True stress-strain data digitized from the tensile test[1], and (b) corresponding true stress-plastic strain curve. Blue solid line is the converted true stress-plastic strain curve and dashed line shows the linear hardening plastic behavior.

3D simulations versus 2D simulations

For the no-hair micro-pillar, we built a three-dimensional (3D) model for the pillar as shown in Fig. S2(a). The dimensions of the pillar were set according to experimental measurement, i.e., square cross-section with a tapered lateral profile: $6 \mu m$ wide at the base, $3.5 \mu m$ wide at the top, and $10 \mu m$ in height (Fig. S2(a)). The micro-pillar was meshed with 3D continuum element (C3D8RH). The interface behavior between the rigid block and the micro-pillar (including the top and lateral surfaces) was described using the Coulomb friction model with a constant isotropic friction coefficient. The friction coefficient was calibrated using experimental data of the tribology tests. Specifically, Fig. 7 of the main text shows the measured friction force under different applied normal loads for the no-hair, short-hair, and long-hair structures. The data for the no-hair structure below the applied normal load of $1000 \mu N$ during the forward stroke was adopted to calibrate the

friction coefficient for two reasons: 1) it did not involve the buckling effect found for the long-hair structure, and 2) it is reasonable to assume a nearly constant contact area during the test (the top surface remained in contact with the indenter as shown in Fig. 4 of the main text). Therefore, the friction coefficient was calculated as the ratio between the friction force and the applied normal load for the no-hair structure during the forward stroke in Fig. 7. The process yielded a consistent friction coefficient of around 0.4. Note that the friction coefficient calculated using the data point at $1000 \mu N$ applied normal load for the no-hair structure is slightly lower than 0.4 (i.e., around 0.35), which is attributed to the plastic deformation within the micropillar under the large load.

Each simulation consists of 3 steps implemented through the static solver of ABAQUS/Standard. The first step is to bring the rigid block and the micro-pillar into contact under a prescribed normal force. After that, the rigid block is subjected to a forward stroke with a lateral displacement of 5 μ m, followed by a backward stroke with a reverse lateral displacement of 5 μ m. Both the forward stroke and backward stroke are under the same fixed normal force.

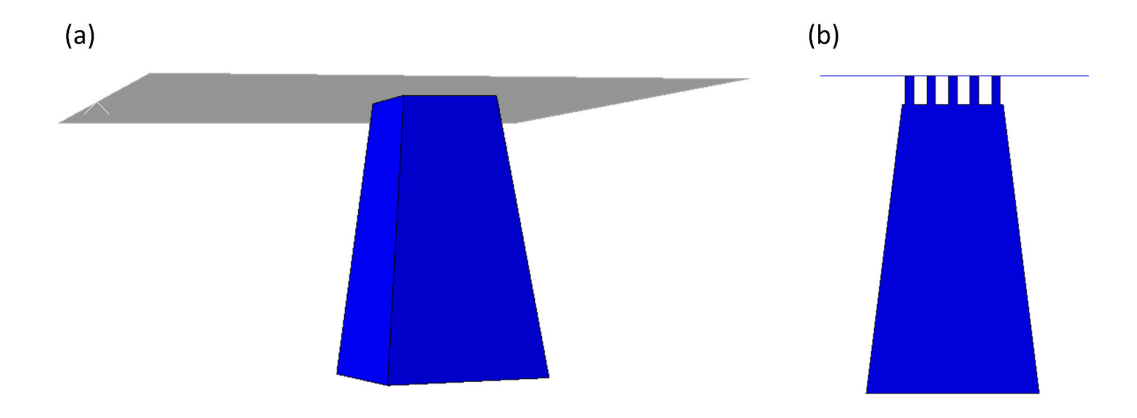


Fig. S2. FEA geometry for (a) 3D flat surface structure, and (b) 2D long-hair structure.

For the short-hair or long-hair structures, much smaller elements are required to accurately simulate the deformation of hair structure, which would result in substantially more elements and hence dramatically increase computational cost and difficulty in convergence of 3D simulations. Therefore, we developed two-dimensional (2D) plane strain models to reduce computational cost. The geometry of the 2D no-hair structure model was a trapezoid (6 µm wide at the base, 3.5 µm wide at the top, and 10 µm in height). The structures with short hairs or long hairs were modelled by adding 5 uniformly spaced rectangles on top of the flat micro-pillar (Fig. S2(b)). The size of each rectangle was 0.3 μ m \times 1 μ m for the long hair structure and 0.3 μ m \times 0.4 μ m for the short hair structure, consistent with the experimental configuration. The same loading process and interface behavior assumed in the 3D simulations were applied to the 2D simulations, except that the prescribed normal force was converted to a line force (force per unit out-of-plane length) by dividing the force by the width of the top surface (3.5 µm) due to the plane strain geometry. For example, the 400 μ N and 1000 μ N normal forces in 3D simulation were converted to 0.1143 N/mm and 0.2857 N/mm, respectively. Correspondingly, the frictional force resulting from 2D simulations was also a line force and was converted to a force by multiplying it with the top pillar width (3.5 µm). The structures (i.e., no-hair, short-hair, or long-hair) were meshed with 2D continuum elements (CPE4RH) and the dynamic implicit solver of ABAQUS/Standard was used to simulate the quasi-static deformation of the structures.

Fig. S3(a) and S3(b) show the frictional force during the forward and backward strokes from 3D and 2D simulations for a no-hair micro-pillar, respectively. Results from the 3D and 2D simulations are very similar, except that for the case of 1000 μN normal force, the frictional force during the forward stroke from 2D simulations is slightly smaller than and not as flat as its

counterpart from 3D simulations. This discrepancy is attributed to the more extensive bending and hence smaller contact area observed in the 2D simulations (see Inset ii in Fig. S3(a) and S3(b)), which results from the difference in a 3D and 2D plane strain geometry as well as the conversion between force (3D) and line force (2D). Nevertheless, the comparison in Fig. S3 shows that 2D simulations are sufficient for capturing the essential features of micro-pillar deformation and its frictional response.

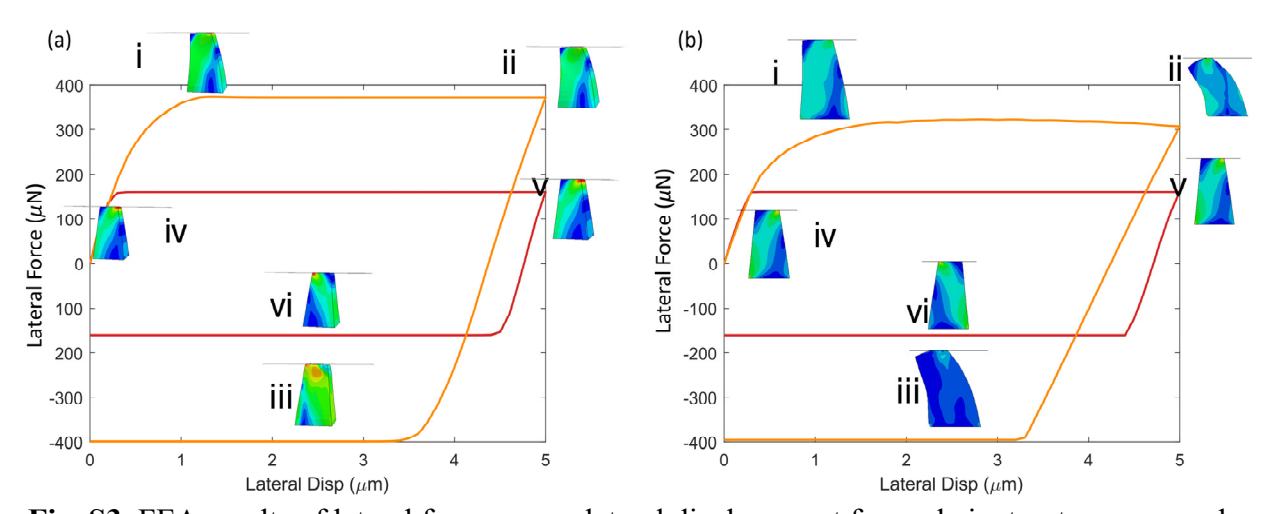


Fig. S3. FEA results of lateral force versus lateral displacement for no-hair structure case under (a) 3D simulation. Insets show the deformation profiles at different lateral displacements. (For $1000\mu N$ loading, the three insets are at lateral displacement = 1, 5, and 2.5 μ m (reverse sliding stroke); for $400 \mu N$ loading, the three insets are at lateral displacement = 0.3, 5, and 2.5 μ m (reverse sliding stroke). (b) 2D plane strain simulation. Insets show the deformation profiles at different lateral displacements. The deformation profiles are extracted at the same time as the 3D simulations.

Dynamic/Explicit solver

For the long-hair structure, the buckling instability occurring under pure normal compression is a highly dynamic process, which may pose challenges to the convergence of the dynamic implicit solver. For example, in the case of long-hair structure under a large normal force (1000 μ N), we observed the development of lateral force even under pure normal loading (see Fig. 6 of the main text), which indicates the buckling of long-hair structure under normal force. Since it is difficult to capture such a buckling instability using the dynamic implicit solver, we used the dynamic explicit solver of ABAQUS/Explicit to perform simulations for the long-hair structure under 1000 μ N normal force. In this model with dynamic explicit solver, the long-hair structure was meshed with CPE4R elements and a uniform mesh size of 0.02 μ m \times 0.02 μ m was used in the entire hair region. To confirm the accuracy of the dynamic explicit solver, in Fig. S4 we compare the results of frictional force for the long-hair structure under 400 μ N normal force obtained from the dynamic implicit and explicit solvers, and the two results agree well with each other, thus we confirmed that these two solvers provided consistent results.

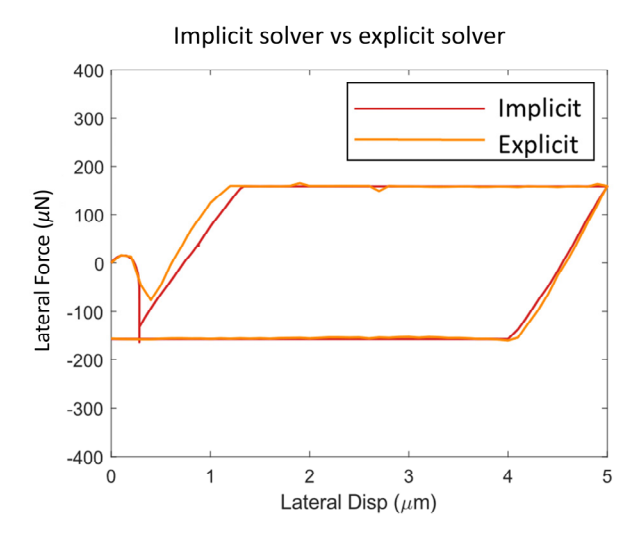


Fig. S4. FEA results of lateral force versus lateral displacement for long-hair structure case under $400 \mu N$ loading with different solvers.

Rescaling the time. The FEA models did not contain any time-dependent parameters in the bulk material or interface models. Also, even though dynamic solvers were adopted to improve convergence, the simulation steps were quasi-static and thus inertial effects were not included. Therefore, the time variable in our simulations is merely a reference for the extent of applied loading and thus can be rescaled without affecting the results. For the 3D static and 2D dynamic implicit simulations, the time for each step of normal loading, forward stroke and backward stroke was 1 s. For the 2D dynamic explicit simulations, the times for loading, normal loading, forward stroke, and backward stroke were 20 s, 100 s and 100 s, respectively, to minimize inertial effects. Although step time is different, the values of normal force and distances of forward and backward strokes were kept the same between the 2D dynamic implicit or explicit simulations. To facilitate direct comparison with experimental data, we rescaled the times of the three simulation steps so that they are in line with the experiments. Specifically, in experiments the normal loading was applied with a rate of 50 µN/s and the forward and backward strokes were applied with a velocity of 0.5 µm/s. Therefore, for the case with 400 µN normal force, it took 8 s for the normal loading step and 10 s each for the forward and backward strokes. For the case with 1000 µN normal force, it took 20 s for the normal loading step and 10 s each for the forward and backward strokes. We proportionally scaled the step time of our stimulation results to be consistent with experiments.

Mesh convergence test

We performed a mesh convergence test for the 2D and 3D models of the no-hair structure as well as the 2D model of the long-hair structure. The mesh sizes for each type of finite element model and results of the mesh convergence test are described in detail in the following paragraphs.

For the 2D model of the no-hair structure, we conducted a mesh convergence test under 1000 μ N normal load for two different meshes, which are referred to as the "fine mesh" and the "coarse mesh." In the fine mesh, the top surface of the micro-pillar base was assigned a uniform mesh size of 0.058 μ m \times 0.05 μ m, which gradually increased to 0.1 μ m \times 0.2 μ m as the bottom surface of the micro-pillar base was approached (see Figure S5b). In the coarse mesh, the top surface of the micro-pillar base was assigned a uniform mesh size of 0.088 μ m \times 0.067 μ m, which gradually increased to 0.15 μ m \times 0.34 μ m as the bottom surface of the micro-pillar base was approached (see Figure S5c). Figure S5a compares the resulting friction force versus lateral displacement obtained from the two meshes. The good agreement confirms that mesh convergence is achieved. The fine mesh was used to obtain the simulation results in Fig.S3.

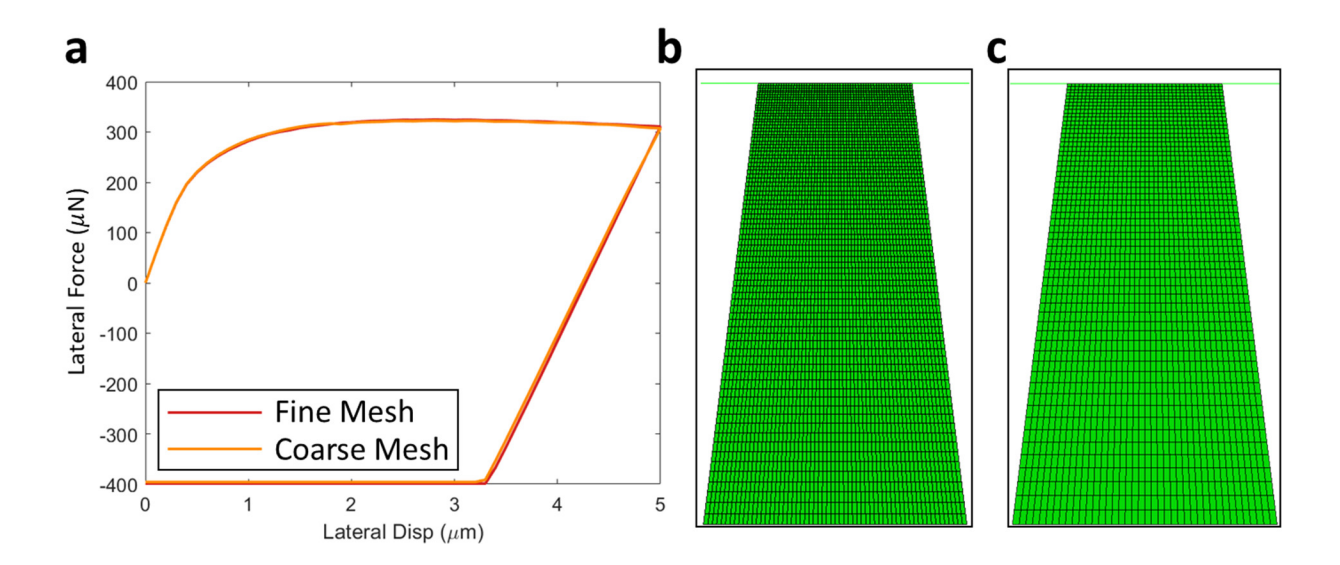


Figure S5. Results of mesh convergence test for the 2D model of the no-hair structure. (a) Lateral force versus lateral displacement under a normal load of 1000 μ N. (b) Fine mesh and (c) coarse mesh of the micropillar.

For the 3D model of the no-hair structure, we also conducted a mesh convergence test under $1000~\mu N$ normal load for two different meshes, which are referred to as the "fine mesh" and the "coarse mesh." In the fine mesh, the top surface of the micro-pillar base was assigned a uniform mesh size of $0.14~\mu m \times 0.14~\mu m \times 0.16~\mu m$, which gradually increased to $0.23~\mu m \times 0.23~\mu m \times 0.81~\mu m$ as the bottom surface of the micro-pillar base was approached (see Figure S6b). In the coarse mesh, the top surface of the micro-pillar base was assigned a uniform mesh size of $0.18~\mu m \times 0.18~\mu m \times 0.20~\mu m$, which gradually increased to $0.29~\mu m \times 0.29~\mu m \times 1.01~\mu m$ as the bottom surface of the micro-pillar base was approached (see Figure S6c). Figure S6a compares the resulting friction force versus lateral displacement obtained from the two meshes. The good agreement confirms that mesh convergence is achieved. The fine mesh was used to obtain the simulation results in Fig.S3.

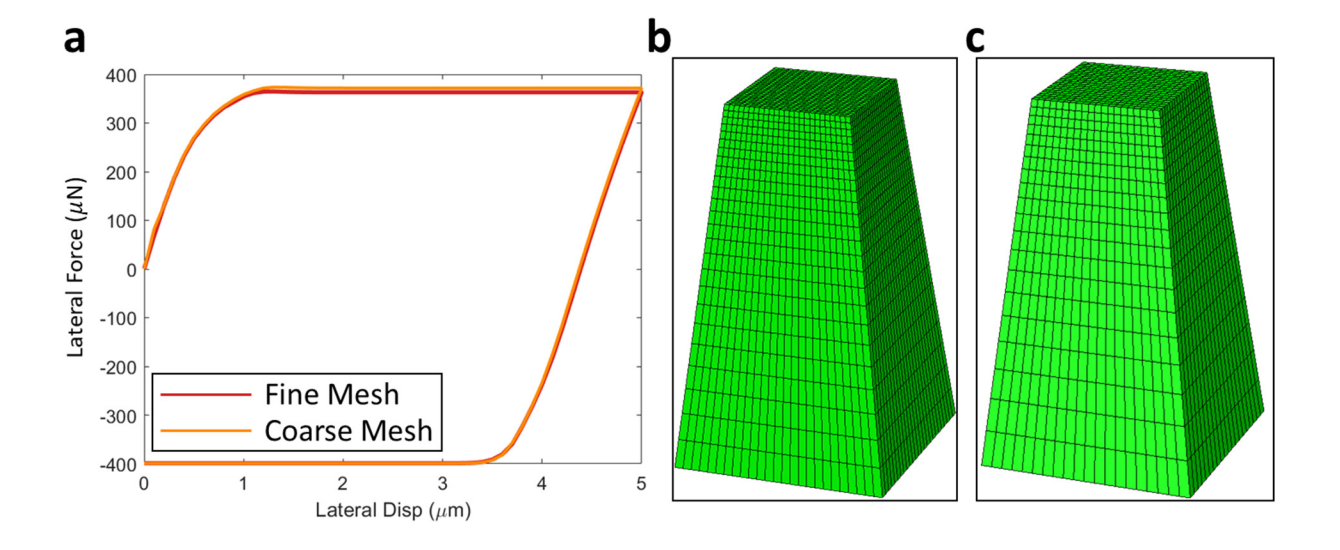


Figure S6. Results of mesh convergence test for the 3D model of the no-hair structure. (a) Lateral force versus lateral displacement under a normal load of 1000 μ N. (b) Fine mesh and (c) coarse mesh of the micropillar.

For the 2D model of the long-hair structure, because of the smaller dimensions of the hairs, a finer mesh was required as compared to the no-hair structure. We conducted a mesh convergence test for the long-hair structure under 400 μ N normal load using the dynamic/implicit solver for two different meshes. These two meshes will be referred to as the "fine mesh" and the "coarse mesh." In the fine mesh, the top surface of the hair was assigned a uniform mesh size of 0.006 μ m \times 0.01 μ m, which gradually increased to 0.03 μ m \times 0.01 μ m as the bottom surface of the hair was approached (see Figure S7b). In the coarse mesh, the top surface of the hair was assigned a uniform mesh size of 0.01 μ m \times 0.02 μ m, which gradually increased to 0.06 μ m \times 0.02 μ m as the bottom surface of the hair was approached (see Figure S7c). Figure S7a compares the resulting friction force versus lateral displacement obtained from the two meshes. The good agreement confirms that mesh convergence is achieved. We adopted the fine mesh for the simulations of the long-hair structure under the 400 μ N normal load using the dynamic/implicit solver.

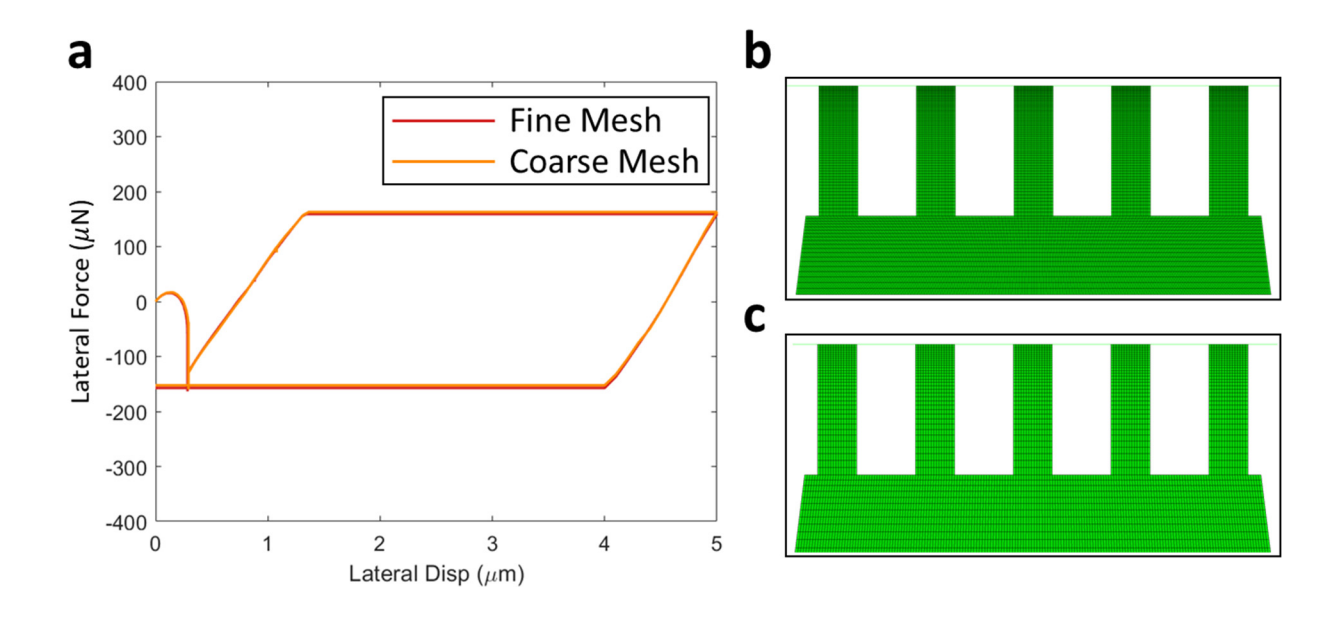


Figure S7. Results of mesh convergence test for the 2D model of the long-hair structure. (a) Lateral force versus lateral displacement under a normal load of 400 μN. (b) Fine mesh and (c) coarse

mesh of the long-hair structure and the top part of the micro-pillar base. The full mesh of the micro-pillar base is not shown to better illustrate the mesh for the long-hair structure.

S2. Supplementary Figure

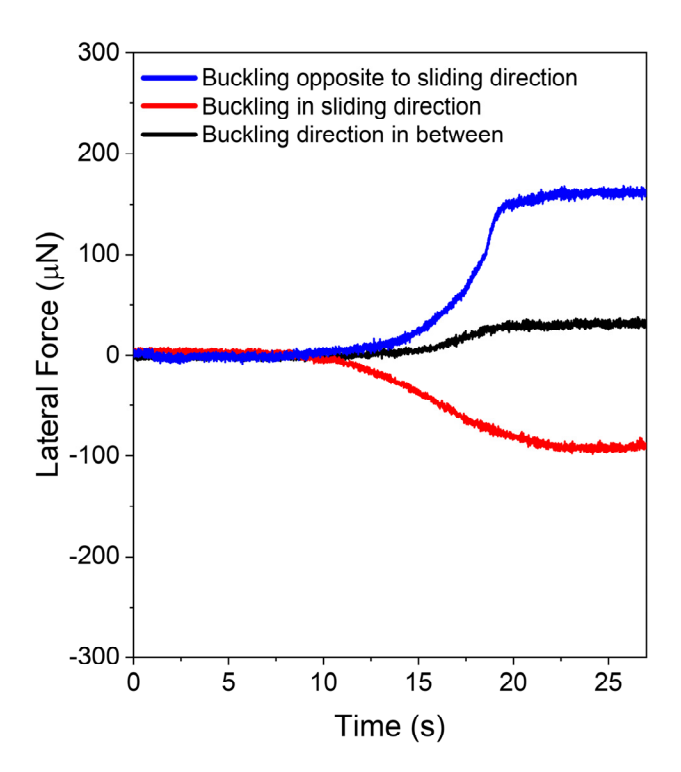


Figure S8. Experimental pre-sliding buckling of long hairs in the direction of, and opposite to counterface sliding direction, resulting in negative and positive lateral forces before sliding, compared to a buckling direction in between the two that resulted in a pre-sliding lateral force closer to zero.

S3. Supplementary Video

Video S1: Recording of the In-Situ SEM testing of the long-hair structure under 400 μ N normal load corresponding to the results shown in Fig. 5(a-d) in the main text.

It should be noted that minor video editing (VSDC Free Video Editor) has been carried out to combine two separate videos into one video file, where each separate video contained different plots (1: lateral load & normal displacement vs time plot, and 2: normal load & lateral displacement vs time plot) and the same live stream of SEM. In the combined video file included here, the first plot is on the top and the second plot is at the bottom. Also, in the SEM live stream included in the video, the areas around the yellow rectangle which are inanimate during the live stream, are masked in white.

References:

[1] Rohbeck N, Ramachandramoorthy R, Casari D, Schürch P, Edwards TEJ, Schilinsky L, et al. Effect of high strain rates and temperature on the micromechanical properties of 3D-printed polymer structures made by two-photon lithography 2020;195:1–9. https://doi.org/10.1016/j.matdes.2020.108977.